Shortwave-Infrared Line-Scan Confocal Microscope for Deep Tissue Imaging in Intact Organs

JAKOB G. P. LINGG,[1,2,*] THOMAS S. BISCHOF,[2]
CHRISTOPHER J. ROWLANDS,[3] OLIVER T. BRUNS,[2,4,5,6] AND
ANDRIY CHMYROV[2,+]

[1]*School of Computation, Information and Technology, Technical University of Munich, Garching, Germany*
[2]*Helmholtz Pioneer Campus, Helmholtz Munich, Neuherberg, Germany*
[3]*Department of Bioengineering, Imperial College London, London, UK*
[4]*Department of Functional Imaging in Surgical Oncology, National Center for Tumor Diseases (NCT/UCC Dresden), Dresden, Germany*
5Technical University Dresden, Dresden, Germany
[6] *Department of Medicine, Technical University of Munich, Munich, Germany*

**jakob.lingg@tum.de*
+andriy.chmyrov@helmholtz-muenchen.de

Abstract: The recent developments of fluorophores having photoemission beyond 1000nm provide the opportunity to develop novel fluorescent microscopes sensitive to those wavelengths. The imaging at wavelengths beyond the visible spectrum allows to achieve imaging depths of hundreds of microns in intact tissue, making this attractive for volumetric imaging applications. Here, a novel shortwave-infrared line-scan confocal microscope is presented that is capable of deep imaging of biological specimens, as demonstrated by visualization of labelled glomeruli in a fixed uncleared kidney at depths of 300µm to 400µm. This development improves the acquisition speed of deep tissue fluorescence imaging.

1. Introduction

One of the current challenges in optical microscopy is the volumetric imaging of intact organs at great depths at high spatiotemporal resolution. Ordinary widefield epifluorescence microscopy, while fast, does not address this challenge as it cannot achieve optical sectioning – the ability of an imaging system to reject background fluorescence originating from outside of the focal plane. While many microscopy techniques [1-6] can achieve optical sectioning, they are often restricted by either imaging depth, spatial- or temporal-resolution, or by the geometry of the sample.

One possibility to improve imaging depths in dense tissue is to shift the detection window to longer wavelengths of the electromagnetic spectrum, such as the shortwave-infrared (SWIR, 1000nm to 2000nm) wavelength regime. The SWIR provides several advantages in terms of light-tissue interactions for optical imaging such as reduced scattering, decreased attenuation by blood and pigments, and lower autofluorescence by tissue [7]. Those properties make it an attractive detection window for optical microscopy. The recent developments of SWIR emissive labels [8-15] paired with the improvement of SWIR sensitive detectors [16, 17] offer the opportunity to develop novel fluorescence microscopes providing optical sectioning that are sensitive to wavelengths beyond 1000nm.

SWIR camera-based systems, such as widefield microscopy, have demonstrated in vivo imaging depths of up to 800µm in the brain through cranial windows [18]. Widefield systems provide high pixel rates of hundreds of gigapixels per second (Gpx/s), however the lack of optical sectioning limits its use to thin or sparsely labelled samples. More advanced methods like light-sheet systems [19, 20] have shown improved optical sectioning by reducing the out-of-focus excitation, nevertheless the off-axis excitation relative to the detection leads to limitations on the possible geometries of samples, making it ineffective for many in vivo applications. In laser-scanning systems, namely confocal and multiphoton, the out-of-focus background is suppressed by either the physical rejection of out-of-focus background by pinholes (confocal) or the non-linear signal generation of multiphoton microscopy. Three-photon microscopy has shown imaging depths in the brain beyond 500µm through skull [21] and depths beyond 1mm through cranial windows [22]. However, as a beam is scanned across the sample in two dimensions, the temporal resolution, especially for larger field-of-views, is low. Moreover, the high photon flux required for three-photon absorption to occur implies lower repetition rates of the laser, typically between 1MHz and 4MHz, compared to the 80MHz repetition rates used in two-photon microscopy. Thus, three-photon microscopy is typically an order of magnitude slower than two-photon microscopy.
SWIR confocal point-scanning systems [16-17, 23-26] have demonstrated imaging depths of 600µm to 1.1mm for various tissues in fluorescence and imaging depths of 1.3mm through cranial windows in the brain in reflectance [26]. However, the reported image acquisition time of the fluorescence confocal systems have been between 5s to minutes per frame [16, 23].

One possibility to increase temporal resolution while maintaining optical sectioning is line-scan confocal microscopy. As the name implies, in line-scan confocal, a tightly-focussed line is scanned across the sample instead of a point; the out-of-focus background is suppressed by a slit or rolling shutter instead of a pinhole [27-29]. Line-scan confocal microscopes reduce the scan time per frame as there is no need to scan the line along its axis, which dramatically improves imaging speed at the cost of a slight degradation in the 3D point-spread function.

Here we demonstrate a novel *de-scanned* shortwave-infrared line-scan confocal microscope (SWIR LSCM) capable of achieving pixel rates of up to 250Gpx/s. The microscope is equipped with an InGaAs line-detector, and is therefore sensitive to shortwave-infrared photoemission of fluorophores. We compare the optical sectioning capabilities of the SWIR LSCM microscope by imaging a liver perfused with fluorescent bacteria on a widefield system and our confocal system. Additionally, we demonstrate the imaging depth of the system by imaging labelled glomeruli in a fixed kidney at depths of 300µm to 400µm.

2. Methods

2.1. Optical configuration

The experimental setup of the SWIR-LSCM is shown in Fig. 1 a). The excitation beam is emitted by a near-infrared fiber-coupled laser (BL976-PAG700, Thorlabs controlled by CLD1015, Thorlabs), this laser beam is collimated by a lens (AC254-075-B-ML, Thorlabs). A cylindrical lens (LJ1640L1-B, Thorlabs) shapes the beam into a line. The beam is reflected upwards by a dichroic mirror (DMLP1000, Thorlabs). After passing a tube lens (TTL200-3P, Thorlabs) and scan lens (SL50-3P, Thorlabs) the beam is scanned by a single-axis silver-coated galvanometer (GVS001, Thorlabs). The beam passes a second pair of scan and tube lenses before forming the illumination line in the back-focal plane the objective (25X XLSLPLN25XGMP NA 1.0, Olympus; with 4:1 glycerol (3783.1, Roth) to water (Millipore) as immersion medium). The fluorescence signal is epi-collected by the high NA objective and de-scanned by the galvanometer. The fluorescence signal passes the dichroic mirror and is spectrally filtered by an emission filter (FELH1000, Thorlabs). An objective lens (4X N4X-PF NA 0.13, Nikon) forms the fluorescence image on the high-speed line-camera (Manx 1024 R,

Xenics) attached to a manual x,z-stage (DTS50/M and PT1/M, Thorlabs). The use of the line-detector removes the need for a slit or a rolling shutter to achieve optical sectioning. To stabilize the temperature of the thermoelectric cooled sensor, we attached a heat sink to the detector and positioned a cooling fan (H17543-001, Intel) close to the detector to be able to image consistently at -10°C detector temperature. While the optical configuration does not lead to diffraction limited imaging and does not make use of the full detector width, the larger field of view paired with lower resolution allows for more fluorescence signal to be collected and enabling faster imaging on the high speed InGaAs line detector.

The galvanometer is driven by a triangular wave generated by a Digital Acquisition (DAQ) card (PCIe-6351, National Instruments). The camera receives two digital signals: the first signal to initialize a frame, followed by signals to trigger acquisition of single lines. The lines are collected and stitched along the y-axis forming a full frame; the scan mechanism is shown in Fig. 2. b.). Frames are acquired for both the forward and backward scan directions to maximize the frame rate.

The z-scanning by the microscope is performed by moving the objective mounted on a fixed-single-objective nosepiece (CSN100, Thorlabs) with a motorized focusing module (ZFM2020, Thorlabs). The electronic components (galvanometer, camera, x,y-stage, z-stage) and the acquisition of stacks is controlled by self-written custom software with a graphical user-interface (Qt C++). The microscope control code is available at GitLab (https://gitlab.com/brunslab/swir-line-scan-confocal).

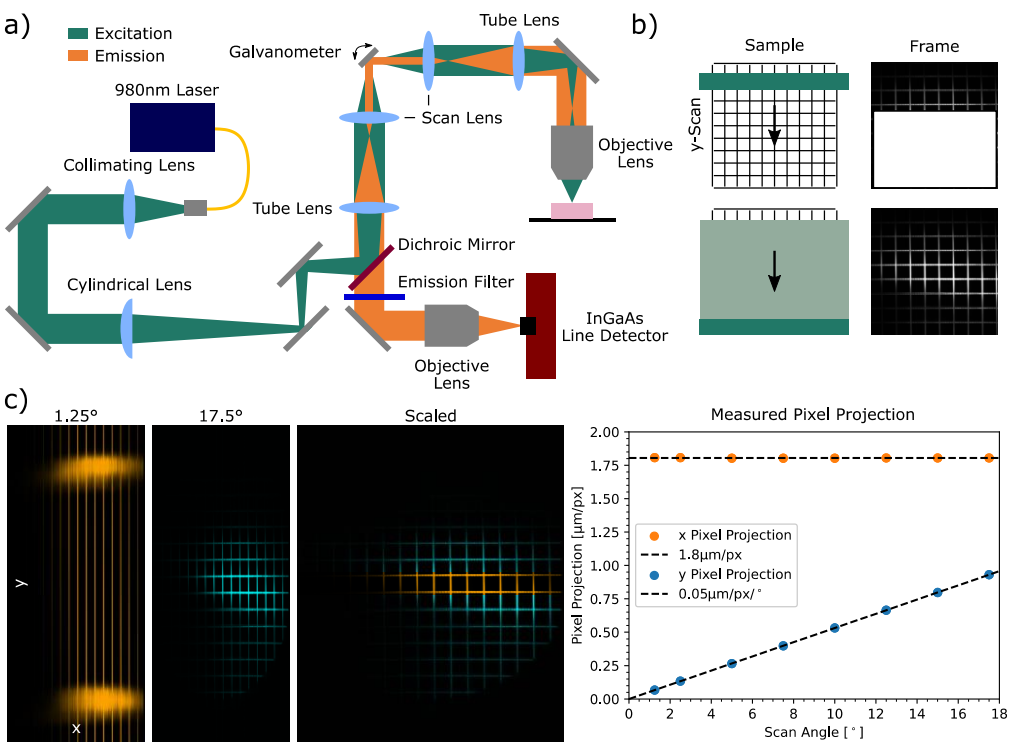

Fig. 1 a) Schematic of SWIR line-scan confocal microscope. b) Explanation of the scan mechanism. A line is scanned from top to bottom (y-axis), the line-detector acquires lines and stitches lines to form the final frame. c) 50µm grid imaged at different scan angles (1.25°, 17.5°), including the overlay of the scaled frames. Plot shows the measured pixel-projection per scan angle for the x- and y-axis.

2.1. Image processing

As the scan range of the galvanometer and the number of lines to be collected per frame can be varied, the resulting images need to be scaled accordingly. Fig. 1. c) displays the frames acquired in reflectance of the same grid (50µm R1L3S3P, Thorlabs) before and after scaling for different scan angles for the same number of lines per frame (1024 lines). The pixel projection per scan angle of the galvanometer is determined by imaging the grid using a variety of scan angles in reflection. The images are background corrected to remove the signal attained from internal reflections. For each background corrected image, the sum along the y-axis and the x-axis is taken. The sums are plotted and the peaks in the image, corresponding to grid lines, are found. The distance between the peaks in pixels corresponds to the known distance of the grid lines, in this case 50µm. Thus, we find the pixel projection per frame in the x- and y-axis. We fit a constant to the pixel projection in the x-dimension per scan angle and a linear function to the y-dimension pixel projection per scan angle. The x-axis pixel projection corresponds to the theoretical pixel projection of 1.8 µm/px. The y-axis pixel projection per scan angle is 0.05 µm/px/°. With those coefficients the acquired images can be scaled for any scan angle.
Data exploration was done using ImageJ. Data processing, analysis, and plotting was performed with Python.

2.2. Resolution

Due to the lack of commercially available point-sources (fluorescent beads, etc.) with photoemission beyond 1000nm, we estimated the resolution of the microscope by measuring SWIR fluorescent bacteria (*blastochloris viridis*, DSM no. 133, DSMZ) [30] embedded in agarose. From a widefield image (IX83, 100X UPLXAPO100X NA 1.45, Olympus; Imaging Source DFK MKU226-10x22) of the crystal violet-stained bacteria (Fig. 2. a)), we estimate the length of a single bacterium to be between 1.5 and 2.5µm, the width is estimated to be between 0.5µm and 0.8µm. A vial with bacteria in medium (Rhodospirillaceae medium no. 27, DSMZ) was centrifuged, the excess medium removed, and Dulbecco's Phosphate Buffered Saline DPBS (14190-094, Gibco) was added to the bacteria. The bacteria solution was vortexed for several minutes until no bacteria clusters were visible in the solution. Bacteria solution was mixed with 1% agarose solution in a 35mm glass bottom dish (81218-200, Ibidi). Once the agarose-bacteria mixture solidified, the glass bottom dish was attached to a custom 3D-printed container which then was filled with the immersion medium (4:1 glycerol (3783.1, Roth) to water (Millipore)).

A stack with axial step size of 0.5µm was acquired. The stack was dark corrected, before being normalized for bleaching by dividing the frames with the average frame value of the section; this assumes a homogenous and isotropic distribution of bacteria (a maximum intensity projection of the first 50µm depth is shown in Fig. 2. b)). A rolling ball background correction with radius 10px was then applied. A Gaussian curve was fitted through the values of the line-profiles passing through the brightest spot of the bacteria sub-stack. The full-width half-maximum of the y-axis resolution (confocal direction) was measured to be 1.6µm, the z-resolution to be 5.3µm (Fig. 2. e)).

2.2. Bacterial Spectra

The absorption spectrum of the fluorescent bacteria (Fig. 2. c)) was measured with a UV/VIS/NIR spectrophotometer (PerkinElmer Lambda1050+) equipped with a 150mm WB-InGaAs (wideband) integration sphere (L6020364, PerkinElmer). We measured the spectrum of the bacteria in medium in a plastic cuvette (Hach 2629500, 10mm path length, 1.5mL); the acquired spectrum was corrected by subtracting the spectrum of the pure medium.

We measured the emission spectrum of the bacteria in medium using a liquid nitrogen cooled InGaAs line-detector (Princeton Instruments Pylon-IR 1024-1.7) attached to a Czerny-Turner spectrograph (Princeton Instruments HRS-300). The sample was excited with 785nm

wavelength (SuperK-Extreme, NKT Photonics filtered with SR-Extended-8HP LLTF Contrast, NKT Photonics). Additionally, the excitation light was spectrally filtered by short-pass filters (FESH0800, Thorlabs) and focused on to the mounted cuvette by an achromat (AC254-200-AB-ML, Thorlabs). The photoemission was collected using a pair of silver-coated off-axis parabolic mirrors (MPD269-P01 and MPD269-P01-H, Thorlabs) that focus the light onto a multimode fiber (400µm, 0.39 NA, M28L01, Thorlabs) that enters the spectrograph. Two long-pass filters (FELH0850, Thorlabs) were placed in front of the fiber to suppress the excitation light. Acquired spectra were background corrected and intensity corrected using a calibration lamp (SLS201L/M, Thorlabs), considering the quantum efficiency of the detector and wavelength dependent transmission losses of the system components. The spectrum was wavelength binned and normalized for the excitation power of 4mW at the sample, resulting in a spectrum in units of counts per wavelength per number of excitation photons.

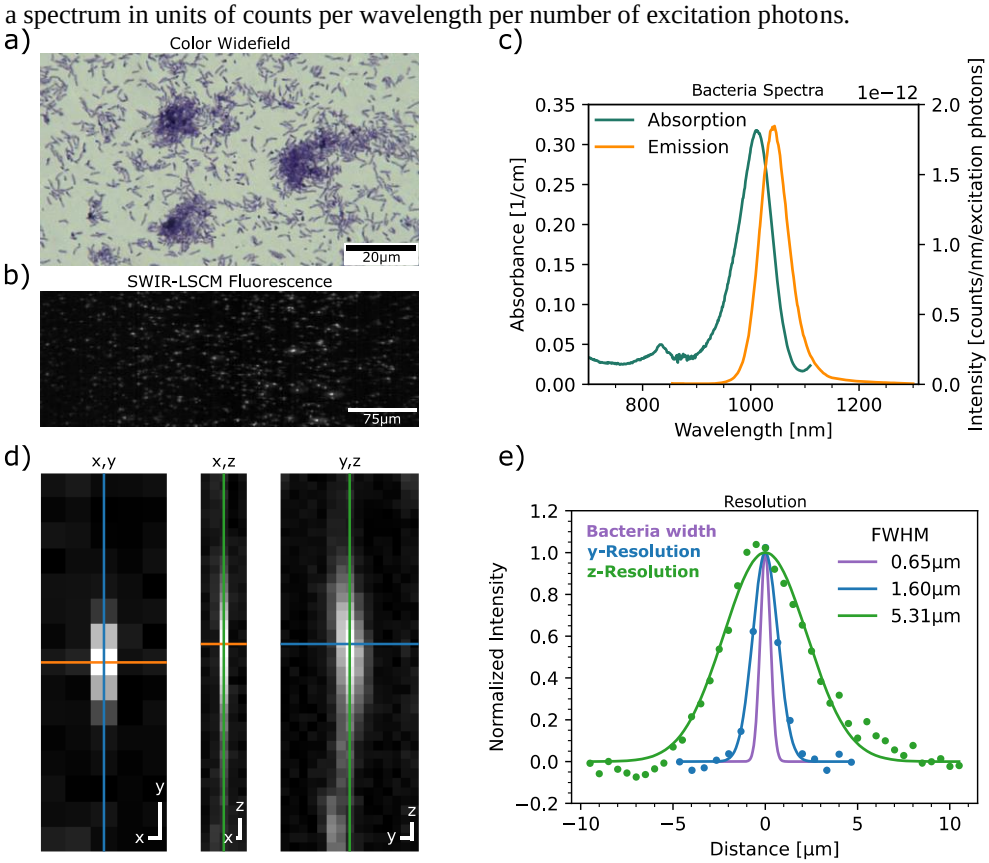

Fig. 2 a) Blastochloris viridis stained with crystal violet (IX83 with 100X UPLXAPO100X NA 1.45, Olympus; Imaging Source DFK MKU226-10x22). b) SWIR-LSCM acquired maximum intensity projection of 50µm of bacteria embedded in agarose. c) Absorption and emission properties of the the bacteria. d) Image planes of single bacterium imaged with SWIR-LSCM as resolution estimate. e) Resolution estimate plot including the bacterium size as the width of a stained bacterium (purple line), resolution measurement in x-dimension (blue line), and the resolution measurement in z-dimension (green line).

2.3. Animal preparation

A mouse (Athymic Nude (Crl:NU(NCr)-*Foxn1*^{nu}), female, 7 weeks, Charles River) was anesthetized with an i.p. Ketamin Xylazin injection. The blood was flushed out by perfusing the mouse with heparin in PBS (20U/ml, 375095-100KU, Merck) through the heart using a

continuous flow syringe pump (4ml/min, 4000-X, Chemyx). Afterwards, 7.5ml *blastochloris viridis* in PBS (14190-094, Gibco) was flushed through the vasculature using the syringe pump. Organs were extracted and fixed in Paraformaldehyde solution 4% in PBS (SC-281692, Santa Cruz Biotechnology).

2.4. Widefield imaging

We used an inverted widefield microscope (IX83, Olympus) with an InGaAs detector (Nirvana HS, Teledyne or Goldeye-034, Allied Vision) to make the comparison between the SWIR-LSCM and the widefield system (Fig. 3). The microscope was used to image the cryo-sliced sections of the kidney (Fig. 4 c)) in fluorescence and brightfield configuration (absorption contrast). Excitation light of a near-infrared laser (980nm, LU0980D350-U30 AF, Lumics) was coupled via a 30:70 beamsplitter (BS020, Thorlabs) to a light guide into the microscope body. The filter cube used consists of a 1000nm short-pass filter (FESH1000, Thorlabs), dichroic mirror (DMLP1000), and a long-pass filter (FELH1050) in the detection path.

3. Results

3.1. Comparison to Widefield Microscopy

We evaluated the optical sectioning capabilities of the SWIR LSCM by imaging the same structure in a fixed mouse liver labelled with fluorescent bacteria on a widefield system and the confocal system. We embedded the liver in agarose in a 35mm glass bottom dish (81218-200, Ibidi) to simplify the transition and correlation between the inverted widefield system (20X UPLXAPO20X NA 0.8, Olympus) and the epi confocal system. A thin and narrow tape was stuck on top of the cover glass as orientation, allowing to align the positions of the sample in both systems via brightfield imaging on the widefield system and reflectance imaging on the confocal.

We matched the pixel projection of the widefield system of ~1µm/px by adjusting the scan angle of the confocal system.

Both stacks were background and flat corrected. The acquired frames had sufficient signal to noise, therefore no additional rolling ball background subtraction was applied. From the images alone, here normalized to minimum and maximum values, the contribution of the out-of-focus background is noticeably stronger in the widefield images compared to the confocal images. Vertical line-profiles normalized to the maximum were plotted, indicating that the contrast in the confocal images is approximately a factor of three greater than the widefield system.

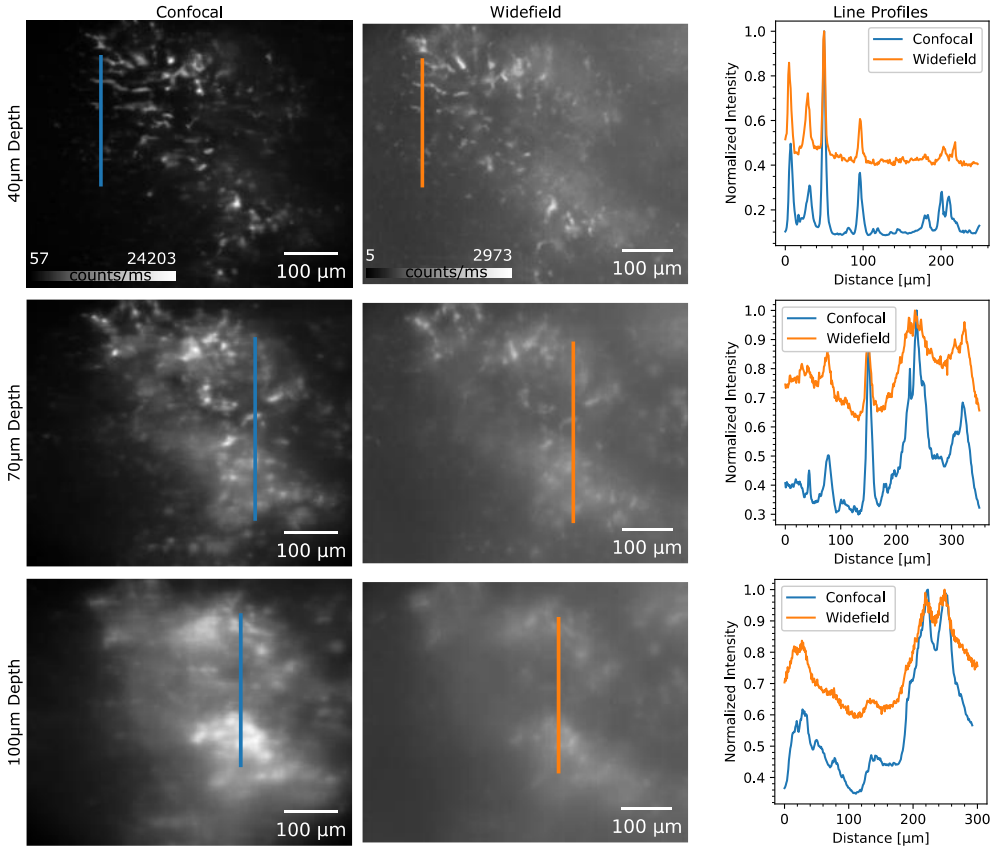

Fig. 3. Left and center columns: Images of mouse liver perfused with bacteria at different depths taken with both the SWIR-LSCM and the widefield system. The colorbar indicates the signal in counts per exposure time; the line exposure time for the SWIR-LSCM was 2.2ms and the widefield exposure time was set to 20ms. Right column: Intensity-normalized line profiles as shown in the SWIR-LSCM and widefield images.

3.2. Organ Imaging

To further understand the capabilities of the SWIR-LSCM, we imaged a fixed kidney perfused with *blastochloris viridis*. The bacteria accumulated in the glomeruli, the structure in which blood is filtered. We were able to image glomeruli at depths of 300 to 400µm within the fixed kidney. The dark-corrected frames at depths of steps of 100µm are shown in Fig. 4. a). Additionally, we selected ROIs of glomeruli and measured the contrast, in this case the mean over standard deviation of counts, within the selected ROI throughout the stack. The resulting contrasts are plotted in Fig. 4. b). From the plot we can see that the glomeruli show their highest contrast at different depths, highlighting again the optical sectioning capabilities of the instrument. In the purple ROI, a vessel is located at a depth of 100µm, this contrast is also visible in the contrast plot. The diameter size of the glomeruli of between 40µm to 100µm and the position of the glomeruli at depths beyond 200µm from the kidney surface corresponds to known literature values [31]. We color coded the slices of the stack according to the depth [32] and performed a maximum intensity projection (MIP) of the colored stacks. This allows us to see the contributions of partly-labelled vessels close to the surface of the kidney.

We confirmed that we were able to label glomeruli with bacteria by imaging cryo-sliced sections of the kidney in fluorescence on the widefield system (4X UPLAXAPO4X NA 0.16, Olympus), the acquired tiles were dark corrected and stitched [33], further we overlayed the

stitched brightfield image of the kidney (Fig. 4. c)). Afterwards, we performed hematoxylin and eosin (H&E) staining with the same section (Fig. 4. d)); the round darker structures are the glomeruli. The zoomed sections of the H&E-stained slice and the fluorescence slice indicates that we were able to label the glomeruli and ultimately confirms that we can image deep within the dense structure of the kidney and resolve glomeruli with our microscope.

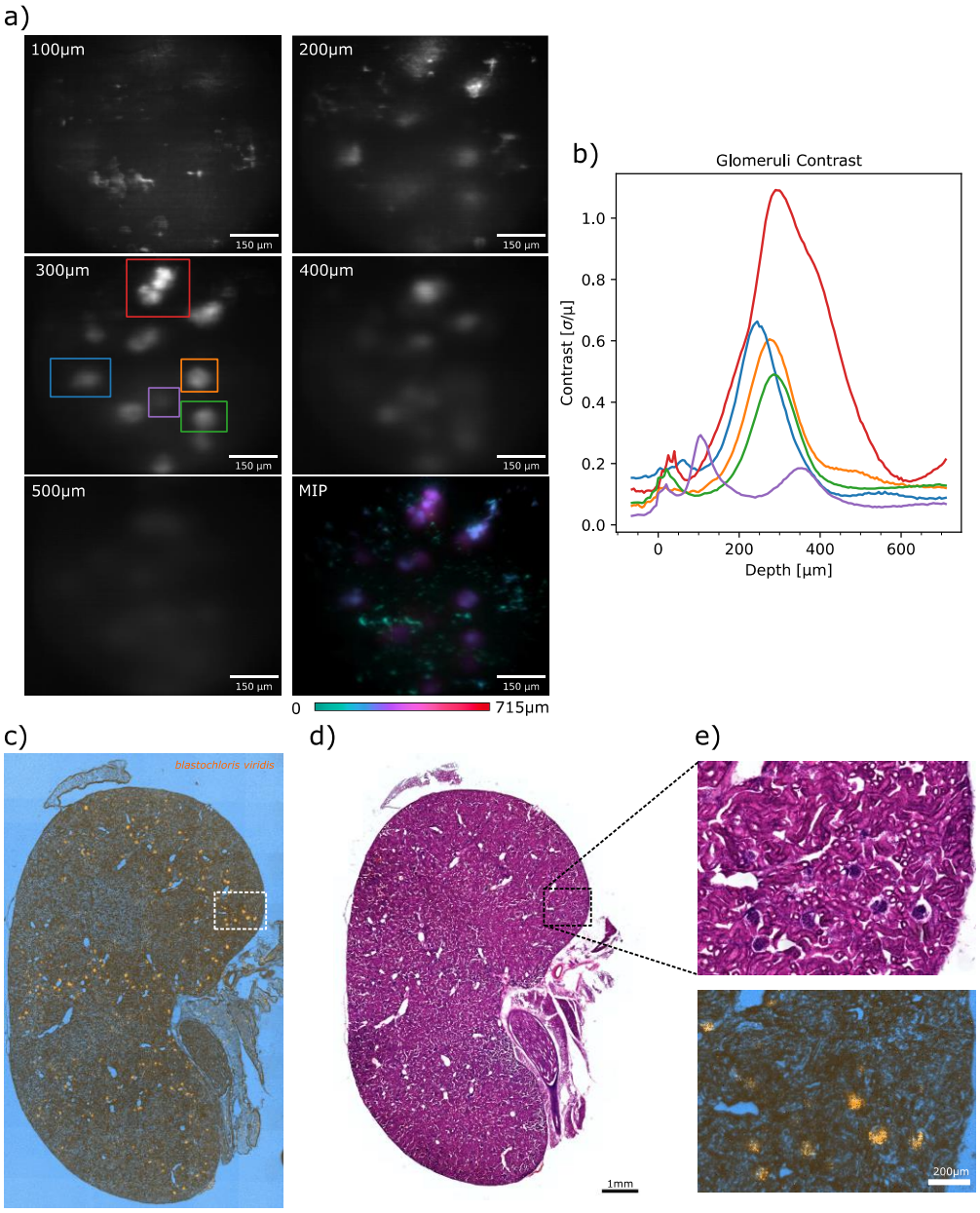

Fig. 4. a) Sections of intact fixed kidney imaged with SWIR-LSCM; the line exposure was set to 4.4ms, this corresponds to an imaging speed of 5s per frame. For the 300µm depth image, ROIs have been drawn over certain glomeruli. MIP: max intensity projection (MIP) of z-colored stacks. b) Contrast measured within the ROIs throughout the stack. c) Overlay of brightfield and fluorescence image of kidney cryo-section. d) H&E-stained cryo-section including zoom selection. e) Zoom of H&E-stained slide including

the corresponding fluorescence and brightfield overlay showing glomeruli at around 200µm under the surface.

4. Discussion

We developed a microscope that can image hundreds of microns deep into fixed uncleared tissue, which opens many new opportunities in terms of deep tissue imaging in intact dense organs. In addition to the penetration depth, the opportunity to image at high spatio-temporal resolution makes this microscope viable for in vivo imaging. However, this requires bright fluorophores and sensitive detectors, as the speed of our current system is limited by the comparatively-high noise floor of the InGaAs detector relative to the noise levels of standard silicon detectors and not yet by the scanning speed of the galvanometer or the line-rate of the camera. The quality of the images could be improved by deconvolving the images using the asymmetric acquired point-spread function.

When compared to multiphoton microscopy, the SWIR-LSCM does provide more penetration depth compared to our two-photon measurements in a fixed kidney of up to 200µm (see Supplementary Figure 1), which are in line with reported two-photon measurements (~200µm) in kidneys [34]. The linear excitation of the line-scan confocal system leads to larger contributions of out-of-focus excitation, where the laser excitation is sufficient to excite the fluorophores in superficial structures of the tissue, even though it is not focused on this position, reducing the image contrast. Such loss of contrast is also forming a limit for achievable imaging depths in multiphoton microscopy [35]. In addition, multiphoton processes suffer from loss of efficiency due to pulse broadening by dispersion, which does not affect single photon excitation in confocal microscopy. The imaging speed of the multiphoton systems, as any point-scanning technique, is limited by the scanning speed of the beam scanners and emission rates from the labels. Thus, the field-of-view must be restricted to be able to image at high temporal resolution. We overcome this issue by parallelizing the acquisition on a line-detector. Generally, our microscope is more cost-effective and easier to implement compared to multiphoton microscopes. Further, line-scan confocal achieves superior optical sectioning capabilities compared to multi-spot confocal and spinning disk confocal systems [36].

SWIR-LCSM is a new technique and there are a variety of improvements which could be made. Adding more excitation wavelengths to enable the use of multiple fluorophores via excitation multiplexing in the SWIR [11] and the addition of a reflectance channel would improve the usability of the instrument. The installation of the reflectance channel would require the adding of polarizing optics to suppress the contribution of internal reflectance arising from the optics [26], potentially leading to transmission losses. To make more use of the detector width of the InGasAs line-detector and to be able to increase the pixel projection [µm/px], a different imaging lens at the detector could be used, for example a 2.5X objective would lead to a pixel projection of 1.1µm/px, or a lens with a focal length of 300mm would lead to 0.67µm/px pixel-projection. However, as we are currently signal starved, we did not reduce the pixel-projection in our system. As the SWIR spectral range is not commonly used in microscopy, additional care needs to be taken of the transmission properties of all optical components.

In conclusion, SWIR-LSCM provides an imaging speed increase of at least a factor two over point-scanning systems. We achieved pixel rates of 100kpx/s with a detector gain setting of 20× and only using half of the detector width. Using the same fluorescent label, we can even improve the imaging speed further by increasing the detector gain to 100×, leading to pixel rates of 500kpx/s while tolerating increased noise levels. Comparable SWIR confocal systems [16, 23] report pixel rates between 5kpx/s and 50kpx/s in fluorescence. Thus, we believe that with the current state of SWIR photoemissive labels and SWIR sensitive detectors, the line-

scan imaging configuration is the most viable option to perform optical sectioning in the SWIR with potential dynamic imaging applications in mind.

Funding. We acknowledge funding from the Helmholtz Zentrum München, the DFG-Emmy Noether program (no. BR 5355/2-1) and from the CZI Deep Tissue Imaging (DTI-0000000248). J. Lingg is supported by funding from the Joachim Herz Foundation.

Acknowledgments. We thank Hannes Rolbieski for the support with the animal handling and mouse perfusion. Further, we thank David Kamel for the support with the bacteria culture.

Disclosures. The authors declare no competing financial interests.

Data availability. Datasets, including all raw and processed imaging data generated in this work, will be made available at the BioImage Archive with the publication.

Code availability. Source code for the microscope control is available at https://gitlab.com/brunslab/swir-line-scan-confocal. The processing and analysis scripts are available at https://gitlab.com/brunslab/manuscript-swir-line-scan-confocal.

References

[1] J.-A. Conchello and J. W. Lichtman, "Optical sectioning microscopy," *Nature Methods*, vol. 2, p. 920–931, November 2005.

[2] F. Helmchen and W. Denk, "Deep tissue two-photon microscopy," *Nature Methods*, vol. 2, p. 932–940, November 2005.

[3] J. Mertz, "Optical sectioning microscopy with planar or structured illumination," *Nature Methods*, vol. 8, p. 811–819, September 2011.

[4] D. Lim, K. K. Chu and J. Mertz, "Wide-field fluorescence sectioning with hybrid speckle and uniform-illumination microscopy," *Optics Letters*, vol. 33, p. 1819, August 2008.

[5] E. H. K. Stelzer, F. Strobl, B.-J. Chang, F. Preusser, S. Preibisch, K. McDole and R. Fiolka, "Light sheet fluorescence microscopy," *Nature Reviews Methods Primers*, vol. 1, November 2021.

[6] C. Dunsby, "Optically sectioned imaging by oblique plane microscopy," *Optics Express*, vol. 16, p. 20306, November 2008.

[7] G. Hong, S. Diao, J. Chang, A. L. Antaris, C. Chen, B. Zhang, S. Zhao, D. N. Atochin, P. L. Huang, K. I. Andreasson, C. J. Kuo and H. Dai, "Through-skull fluorescence imaging of the brain in a new near-infrared window," *Nature Photonics*, vol. 8, p. 723–730, August 2014.

[8] V. G. Bandi, M. P. Luciano, M. Saccomano, N. L. Patel, T. S. Bischof, J. G. P. Lingg, P. T. Tsrunchev, M. N. Nix, B. Ruehle, C. Sanders, L. Riffle, C. M. Robinson, S. Difilippantonio, J. D. Kalen, U. Resch-Genger, J. Ivanic, O. T. Bruns and M. J. Schnermann, "Targeted multicolor in vivo imaging over 1,000nm enabled by nonamethine cyanines," *Nature Methods*, vol. 19, p. 353–358, February 2022.

[9] O. T. Bruns, T. S. Bischof, D. K. Harris, D. Franke, Y. Shi, L. Riedemann, A. Bartelt, F. B. Jaworski, J. A. Carr, C. J. Rowlands, M. W. B. Wilson, O. Chen, H. Wei, G. W. Hwang, D. M. Montana, I. Coropceanu, O. B. Achorn, J. Kloepper, J. Heeren, P. T. C. So, D. Fukumura, K. F. Jensen, R. K. Jain and M. G. Bawendi, "Next-generation in vivo optical imaging with short-wave infrared quantum dots," *Nature Biomedical Engineering*, vol. 1, April 2017.

[10] J. A. Carr, D. Franke, J. R. Caram, C. F. Perkinson, M. Saif, V. Askoxylakis, M. Datta, D. Fukumura, R. K. Jain, M. G. Bawendi and O. T. Bruns, "Shortwave infrared fluorescence imaging with the clinically approved near-infrared dye indocyanine green," *Proceedings of the National Academy of Sciences*, vol. 115, p. 4465–4470, April 2018.

[11] E. D. Cosco, A. L. Spearman, S. Ramakrishnan, J. G. P. Lingg, M. Saccomano, M. Pengshung, B. A. Arús, K. C. Y. Wong, S. Glasl, V. Ntziachristos, M. Warmer, R. R. McLaughlin, O. T. Bruns and E. M. Sletten, "Shortwave infrared polymethine fluorophores matched to excitation lasers enable non-invasive, multicolour in vivo imaging in real time," *Nature Chemistry,* vol. 12, p. 1123–1130, October 2020.

[12] G. Hong, J. T. Robinson, Y. Zhang, S. Diao, A. L. Antaris, Q. Wang and H. Dai, "In Vivo Fluorescence Imaging with Ag2S quantum dots in the second near-infrared region," *Angewandte Chemie International Edition,* vol. 51, p. 9818–9821, September 2012.

[13] Z. Tao, G. Hong, C. Shinji, C. Chen, S. Diao, A. L. Antaris, B. Zhang, Y. Zou and H. Dai, "Biological Imaging Using Nanoparticles of Small Organic Molecules with Fluorescence Emission at Wavelengths Longer than 1000{\hspace{0.25em}}nm," *Angewandte Chemie International Edition,* vol. 52, p. 13002–13006, October 2013.

[14] K. Welsher, Z. Liu, S. P. Sherlock, J. T. Robinson, Z. Chen, D. Daranciang and H. Dai, "A route to brightly fluorescent carbon nanotubes for near-infrared imaging in mice," *Nature Nanotechnology,* vol. 4, p. 773–780, October 2009.

[15] Q. Yang, Z. Ma, H. Wang, B. Zhou, S. Zhu, Y. Zhong, J. Wang, H. Wan, A. Antaris, R. Ma, X. Zhang, J. Yang, X. Zhang, H. Sun, W. Liu, Y. Liang and H. Dai, "Rational Design of Molecular Fluorophores for Biological Imaging in the NIR-II Window," *Advanced Materials,* vol. 29, p. 1605497, January 2017.

[16] F. Wang, F. Ren, Z. Ma, L. Qu, R. Gourgues, C. Xu, A. Baghdasaryan, J. Li, I. E. Zadeh, J. W. N. Los, A. Fognini, J. Qin-Dregely and H. Dai, "In vivo non-invasive confocal fluorescence imaging beyond 1,700nm using superconducting nanowire single-photon detectors," *Nature Nanotechnology,* vol. 17, p. 653–660, May 2022.

[17] F. Xia, M. Gevers, A. Fognini, A. T. Mok, B. Li, N. Akbari, I. E. Zadeh, J. Qin-Dregely and C. Xu, "Short-Wave Infrared Confocal Fluorescence Imaging of Deep Mouse Brain with a Superconducting Nanowire Single-Photon Detector," *ACS Photonics,* vol. 8, p. 2800–2810, September 2021.

[18] Z. Feng, X. Yu, M. Jiang, L. Zhu, Y. Zhang, W. Yang, W. Xi, G. Li and J. Qian, "Excretable IR-820 for in vivo NIR-II fluorescence cerebrovascular imaging and photothermal therapy of subcutaneous tumor," *Theranostics,* vol. 9, p. 5706–5719, 2019.

[19] F. Wang, H. Wan, Z. Ma, Y. Zhong, Q. Sun, Y. Tian, L. Qu, H. Du, M. Zhang, L. Li, H. Ma, J. Luo, Y. Liang, W. J. Li, G. Hong, L. Liu and H. Dai, "Light-sheet microscopy in the near-infrared II window," *Nature Methods,* vol. 16, p. 545–552, May 2019.

[20] F. Wang, Z. Ma, Y. Zhong, F. Salazar, C. Xu, F. Ren, L. Qu, A. M. Wu and H. Dai, "In vivo NIR-II structured-illumination light-sheet microscopy," *Proceedings of the National Academy of Sciences,* vol. 118, February 2021.

[21] T. Wang, D. G. Ouzounov, C. Wu, N. G. Horton, B. Zhang, C.-H. Wu, Y. Zhang, M. J. Schnitzer and C. Xu, "Three-photon imaging of mouse brain structure and function through the intact skull," *Nature Methods,* vol. 15, p. 789–792, September 2018.

[22] N. G. Horton, K. Wang, D. Kobat, C. G. Clark, F. W. Wise, C. B. Schaffer and C. Xu, "In vivo three-photon microscopy of subcortical structures within an intact mouse brain," *Nature Photonics,* vol. 7, p. 205–209, January 2013.

[23] H. Wan, J. Yue, S. Zhu, T. Uno, X. Zhang, Q. Yang, K. Yu, G. Hong, J. Wang, L. Li, Z. Ma, H. Gao, Y. Zhong, J. Su, A. L. Antaris, Y. Xia, J. Luo, Y. Liang and H. Dai, "A bright organic NIR-II nanofluorophore for three-dimensional imaging into biological tissues," *Nature Communications*, vol. 9, March 2018.

[24] M. Zhang, J. Yue, R. Cui, Z. Ma, H. Wan, F. Wang, S. Zhu, Y. Zhou, Y. Kuang, Y. Zhong, D.-W. Pang and H. Dai, "Bright quantum dots emitting at ∼1,600 nm in the NIR-IIb window for deep tissue fluorescence imaging," *Proceedings of the National Academy of Sciences*, vol. 115, p. 6590–6595, June 2018.

[25] S. Zhu, S. Herraiz, J. Yue, M. Zhang, H. Wan, Q. Yang, Z. Ma, Y. Wang, J. He, A. L. Antaris, Y. Zhong, S. Diao, Y. Feng, Y. Zhou, K. Yu, G. Hong, Y. Liang, A. J. Hsueh and H. Dai, "3D NIR-II Molecular Imaging Distinguishes Targeted Organs with High-Performance NIR-II Bioconjugates," *Advanced Materials*, vol. 30, p. 1705799, February 2018.

[26] F. Xia, C. Wu, D. Sinefeld, B. Li, Y. Qin and C. Xu, "In vivo label-free confocal imaging of the deep mouse brain with long-wavelength illumination," *Biomedical Optics Express*, vol. 9, p. 6545, November 2018.

[27] K.-B. Im, S. Han, H. Park, D. Kim and B.-M. Kim, "Simple high-speed confocal line-scanning microscope," *Optics Express*, vol. 13, p. 5151, 2005.

[28] R. Engelmann, "Faster than real-time: confocal linescan systems provide ideal conditions for millisecond-resolution physiological imaging," *Nature Methods*, vol. 3, p. III–V, October 2006.

[29] Q. Zhong, A. Li, R. Jin, D. Zhang, X. Li, X. Jia, Z. Ding, P. Luo, C. Zhou, C. Jiang, Z. Feng, Z. Zhang, H. Gong, J. Yuan and Q. Luo, "High-definition imaging using line-illumination modulation microscopy," *Nature Methods*, vol. 18, p. 309–315, March 2021.

[30] Z. Chang, C. Liu, S. Zhao, J. Chen, X. Zhang, H. Tian and Q. Sun, "Near Infrared-II Fluorescent protein for In-vivo Imaging," March 2022.

[31] B. D. Hann, E. J. Baldelomar, J. R. Charlton and K. M. Bennett, "Measuring the intrarenal distribution of glomerular volumes from histological sections," *American Journal of Physiology-Renal Physiology*, vol. 310, p. F1328–F1336, June 2016.

[32] E. Katrukha, *Z-stack Depth Color Code*, GitHub.

[33] S. Preibisch, S. Saalfeld and P. Tomancak, "Globally optimal stitching of tiled 3D microscopic image acquisitions," *Bioinformatics*, vol. 25, p. 1463–1465, April 2009.

[34] B. A. Molitoris and R. M. Sandoval, "Intravital multiphoton microscopy of dynamic renal processes," *American Journal of Physiology-Renal Physiology*, vol. 288, p. F1084–F1089, June 2005.

[35] L. Wei, Z. Chen and W. Min, "Stimulated emission reduced fluorescence microscopy: a concept for extending the fundamental depth limit of two-photon fluorescence imaging," *Biomedical Optics Express*, vol. 3, p. 1465, May 2012.

[36] A. G. York, P. Chandris, D. D. Nogare, J. Head, P. Wawrzusin, R. S. Fischer, A. Chitnis and H. Shroff, "Instant super-resolution imaging in live cells and embryos via analog image processing," *Nature Methods*, vol. 10, p. 1122–1126, October 2013.